Revealing the Charge Density Wave Proximity Effect in Graphene on 1T-TaS2

Altvater Michael A. Altvater1
Rutgers, The State University of New Jersey
Sheng-Hsiung Hung
Department of Physics, National Tsing Hua University
nikhil tilak
rutgers
Guohong li
rutgers
Choong-Jae won
Pohang University
Sang-Wook Cheong
Rutgers Center for Emergent Materials and Department of Physics and Astronomy
https://orcid.org/0000-0001-9905-6175
Chung-Hou Chung
National Center for Theoretical Sciences
Horng-Tay Jeng
Department of Physics, National Tsing Hua University, Hsinchu 30013 https://orcid.org/0000-0002-2881-3826
Eva Andrei (eandrei@physics.rutgers.edu)
Rutgers, The State University of New Jersey https://orcid.org/0000-0002-2516-2749

Letter

Keywords:

Posted Date: February 17th, 2022

DOI: https://doi.org/10.21203/rs.3.rs-1356410/v1

Revealing the Charge Density Wave Proximity Effect in Graphene on 1T-TaS_2

Michael A. Altvater[1+], Sheng-Hsiung Hung[2+], Nikhil Tilak[1], Choong-Jae Won[3], Guohong Li[1], Sang-Wook Cheong[1], Chung-Hou Chung[4,5*], Horng-Tay Jeng[2,5*] and Eva Y. Andrei[1*]

[1] Department of Physics and Astronomy, Rutgers, the State University of New Jersey, 136 Frelinghuysen Rd, Piscataway, New Jersey 08854, USA
[2] Department of Physics, National Tsing-Hua University, 101 Guangfu Road, Hsinchu 30013, Taiwan
[3] Laboratory for Pohang Emergent Materials and Max Plank POSTECH Center for Complex Phase Materials, Department of Physics, Pohang University of Science and Technology, Pohang 37673, Korea
[4] National Chiao Tung University, 1001 Daxue Road, Hsinchu 30010, Taiwan
[5]Physics Division, National Center for Theoretical Sciences, Taipei 10617, Taiwan

*Correspomding authors E-mail: chung0523@nycu.edu.tw, jeng@phys.nthu.edu.tw, eandrei@physics.rutgers.edu
[+]Equal contributors

The proximity-effect, a phenomenon whereby materials in contact appropriate each other's electronic-properties, is widely used in nano-scale devices to induce electron-correlations at heterostructure interfaces. Commonly observed proximity-induced correlation effects include superconductivity, magnetism, and spin-orbit interactions. Thus far however proximity-induced charge density wave (CDW) correlated states have remained elusive. This is primarily because they are obscured by screening in 3D metals and by defect scattering at interfaces. Here we report the first observation of a proximity-induced CDW, made possible by employing 2D-materials with pristine and atomically smooth surfaces. Using scanning tunneling microscopy (STM) and spectroscopy (STS) together with theoretical modeling to probe the interface between graphene and a 1T-TaS_2 crystal, we show that interactions induce a CDW within graphene and modify the band structure of 1T-TaS_2. We further show that the mechanism underlying the proximity-induced CDW is driven by short-range exchange interactions that are distinctly different from previously observed proximity-effects.

The isolation and manipulation of atomically thin layered materials provides a ready-made two dimensional electron system [1] whose properties can be tuned by external knobs, such as stress or substrate morphology [2-4], leading to the emergence of correlated electron phases. Distinct from these external knobs, a very powerful approach to manipulate electron correlations in these materials is by contact proximity effects. It is well known that proximitizing materials that host correlated electron phases, such as superconductivity [5] or magnetism [6], with normal metals, induces correlations in the normal metal. These effects are a direct consequence of the quantum mechanical properties of electrons in solids; specifically, the non-local nature of electrons. As quantum particles do not have a well-defined position, electronic states cannot abruptly change from one type of ordering to another at the interface of two materials. Consequently, correlated states persist into the normal metal where scattering events begin to destroy the coherence (and vice versa). In the case of 2D materials where scattering is reduced due to their atomically sharp interfaces, proximity-effects are particularly robust allowing correlated states to persist over long distances. The discovery of graphene and other 2D materials, together with the technology enabling 2D heterostructures has led to the observation of strong proximity effects at the atomic limit including proximity induced superconductivity, magnetism and spin-orbit effects [7-15].

The CDW is yet another quantum many-body state arising from electron correlations, such as on-site Coulomb repulsion and short-ranged anti-ferromagnetic spin-exchange interactions., that is seen in correlated insulators and unconventional superconductors [16] as well as in 2D transition-metal dichalcogenide (TMDs) [17]. However, inducing a proximity effect between a CDW material and a normal metal has remained elusive. This is primarily due to screening in 3D metals and interface defect scattering. As described below, the use of 2D materials that were stacked in an inert atmosphere to avoid interface damage and contamination, together with sensitive local probes providing direct access to the charge distribution in graphene, made it possible to overcome these hurdles.

In this work, we present microscopic evidence of the proximity effect between the CDW material 1T-TaS_2, and graphene. Through scanning tunneling microscopy (STM) and spectroscopy (STS), we show that the charge density modulation in 1T-TaS_2 persists within the contacted graphene layer. By comparing with first-principles calculations based on density-functional theory (DFT), we find that in addition to a global charge-transfer between the two surfaces caused by the relative electron negativity, the proximity induced CDW in graphene is driven by a novel mechanism of short-range exchange interactions mediated by second-order local electron hopping, which is distinctly different from superconducting, magnetic and spin-orbit proximity effects.

1T-TaS_2 is known to exhibit a strongly coupled, commensurate CDW below ~180K involving 13 unit cells where 12 of 13 Ta atoms displace from their high-temperature, equilibrium positions toward the central, 13th Ta atom. This lattice displacement and corresponding charge density modulation repeat periodically within each layer to form a triangular super-lattice with period of $\sqrt{13}$ unit cells of 1T-TaS_2. Fig. 1(a) left panel shows the $\sqrt{13} \times \sqrt{13}$ CDW reconstructed 1T-TaS_2 supercell. As shown in Fig. S3, the origin of the CDW formation in 1T-TaS_2 is the Kohn anomaly in the acoustic branch of the phonon spectrum along the Γ→M direction with the phonon frequency critically suppressed by electron-phonon interaction [18,19], leading to the static displacement of the lattice with the wavevector $\mathbf{Q_{CDW}}$ corresponding to the $\sqrt{13} \times \sqrt{13}$ CDW reconstruction. This soft phonon mode at the Kohn anomaly wavevector $\mathbf{Q_{CDW}}$ consists primarily of longitudinal vibrations of Ta atoms with a minor contribution from transverse vibrations of S atoms relative to the phonon propagating direction $\mathbf{Q_{CDW}}$. The star-of-David atomic arrangement involves the local lattice contraction around the center of the star, in which the bond lengths between Ta ions are shorter than those between Ta ions outside the star. To compare with STM images, we calculated the partial charge density of the two lowest energy bands as shown in Fig. 1(a) right panel. The electron cloud mainly distributes over the stars with the highest charge density enhancement of ~5x10^{-3} e/Å^3 locating at the center Ta ion of the star.

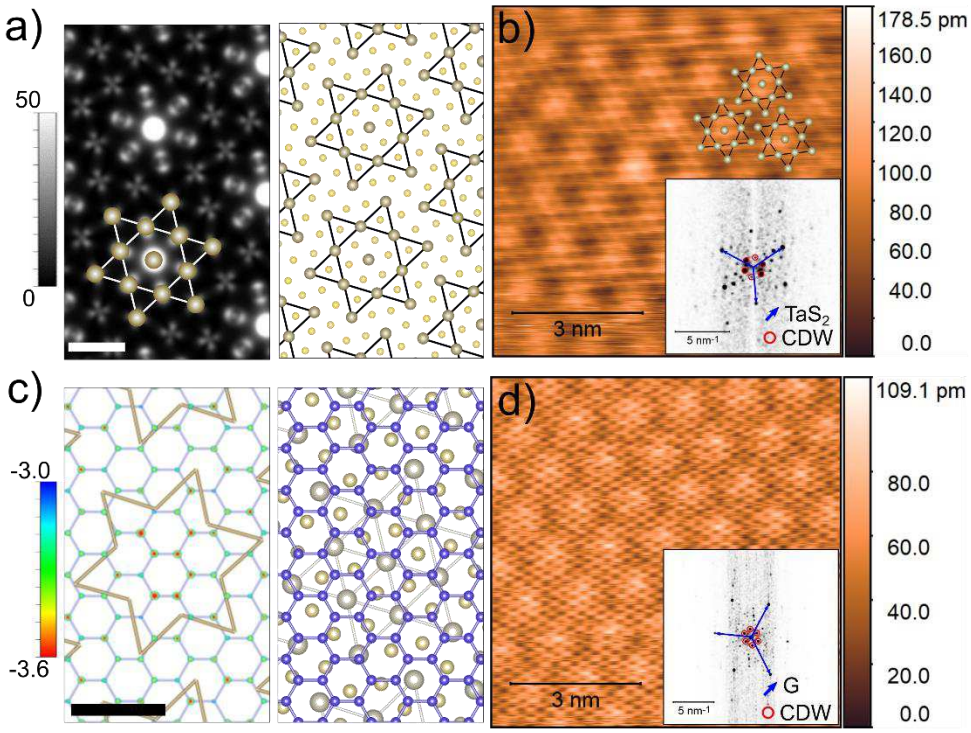

Figure 1 STM Topography of Bare and Encapsulated 1T-TaS2: a) Right panel: Ball and stick model of the $\sqrt{13} \times \sqrt{13}$ CDW reconstructed 1T-TaS_2 lattice with David star clusters outlined. Left panel: DFT computed charge density of the two lowest energy bands in the commensurate CDW. Scale bar is 5Å. Color scale units are 10^{-4}e/ Å^3. b) STM topography of bare surface of 1T-TaS_2 shows the CDW charge modulation as well as the atomic lattice of the 1T-TaS_2 top layer (Ta positions marked with beige dots) (V_b=1.2V, I_{SP}=40pA) inset: FFT of topography image shows Bragg peaks from the lattice as well as the CDW modulation. c) Right panel: Ball and stick model of graphene placed on 1T-TaS_2 in the commensurate phase. Left panel: DFT computed charge transfer of the graphene layer (the charge density of pristine graphene is subtracted from the charge density of the graphene layer on 1T-TaS_2) shows a local modulation of doping with the periodicity of the CDW of TaS_2. The pattern of the colored dots indicate stronger hole doping in graphene around the David stars. Scale bar is 5Å. Color scale units are 10^{-4}e/ Å^3. d) STM topography of graphene placed on 1T-TaS_2 shows both the graphene lattice as well as the super-lattice charge density modulation associated with the CDW of 1T-TaS_2 inset: FFT of topography image shows Bragg peaks from the graphene lattice as well as the CDW modulation.

Experimentally, the charge density modulation is evident in the STM topography image of the bare 1T-TaS_2 surface, Fig. 1(b). The STM measures both the density of states (DOS) modulation due to the CDW reconstruction and the positions of the sulfur sub-lattice. This can be seen in the fast Fourier transform (FFT) [Fig. 1(b) inset] which shows Bragg peaks associated with the 1T-TaS_2 lattice spacing (blue arrows) as well as peaks corresponding to the CDW wavevectors (red circles). The $\sqrt{13} \times \sqrt{13}$ CDW reconstruction is depicted as star-shaped clusters of Ta atoms in Fig. 1(b).

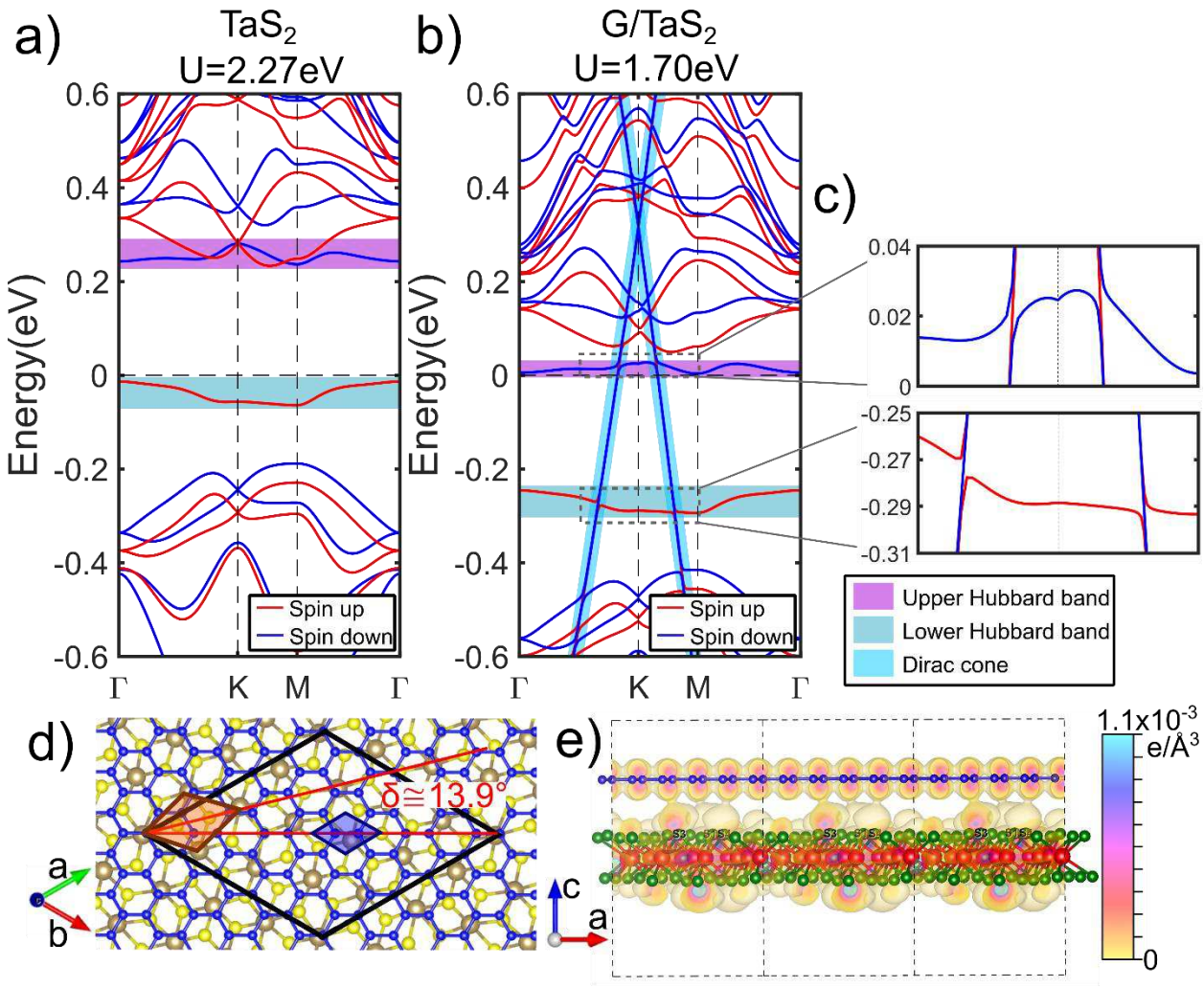

Figure 2: Band Structureof 1T-TaS2 and G/TaS$_2$ a) GGA+U band structure of $\sqrt{13} \times \sqrt{13}$CDW reconstructed 1T-$TaS_2$ with U=2.27eV. Hubbard bands, associated with the localized electronic state at the center of the David stars, are highlighted. b) GGA+U band structure of G/TaS_2 using a phenomenological value U=1.70eV. Owing to the charge transfer from graphene to 1T-TaS_2, the Fermi level (zero energy) moves from the lower Hubbard band to the upper Hubbard band, and the graphene-associated Dirac point at the K-point of the superstructure Brillouin zone is shifted to ~ 0.3eV above the Fermi level (E_F) indicating hole doping. The hole distribution [Fig. 1(c)] forms the real space modulation in graphene with the same periodicity as the underlying √13×√13 CDW of 1T-TaS_2 through the proximity effect. Hubbard bands and Dirac cone are highlighted for clarity. c) Zoomed in view of the crossing points between the Dirac cone and Upper (top) and Lower (bottom) Hubbard bands. d) Top view of G/TaS_2 heterostructure. Blue, brown, and yellow spheres indicate C, Ta, and S atoms, respectively. Black, blue, and brown rhombuses show the 5x5 G/$\sqrt{13} \times \sqrt{13}$$TaS_2$ supercell, graphene 1x1 unit cell, and 1T-TaS_2 1x1 unit cell, respectively. The graphene and TaS_2 layer are twisted by ~13.9° in this CDW phase. e) Side view of G/TaS_2 heterostructure overlaid with the charge density map (bubble-shaped color contour indicating the electron density) corresponding to the states at the two crossing points of the Dirac cone and Lower Hubbard band. The slight overlap between graphene and 1T-TaS_2 electron clouds give rise to

the interlayer coupling and proximity effect. Here, blue, red, and green spheres represent C, Ta, and S atoms, respectively.

First-principle electronic structure calculations were performed using the projector augmented wave (PAW) approach within the framework of density functional theory (DFT) as implemented in the Vienna ab initio Simulation Package (VASP) [20-23]. The exchange-correlation is described in the Perdew-Burke-Ernzerhof (PBE) form of generalized gradient approximation (GGA) [23,24]. Fig. 1(c) right panel shows the top view of the graphene/TaS_2 (G/TaS_2) heterostructure used in the DFT calculation [The supercell structure is shown in Fig. 2(d)]. By subtracting the calculated charge density of freestanding graphene monolayer from the charge density of G/TaS_2, Fig. 1(c) left panel illustrates the 1T-TaS_2 induced local doping in the graphene cover layer. From the induced charge density map, we observe a negative induced charge density of ~0.00036 holes/ $Å^3$ near the centers of the David stars in the 1T-TaS_2 layer below (local hole doping). The induced charge density modulation in the graphene layer shows the same periodicity as the CDW in 1T-TaS_2 layer with the strongest charge transfer located around the center of the 1T-TaS_2 CDW stars with the strongest CDW potential, demonstrating the correlation between graphene and 1T-TaS_2. Indeed, STM topography measurements of the top graphene layer in a G/TaS_2 heterostructure also reveal a strong intensity modulation of graphene's honeycomb lattice with a period that matches that of the CDW in 1T-TaS_2 [see Fig. 1(d)]. The two-dimensional periodic modulation is evident in the fast Fourier transform (FFT) of the topography image [Fig. 1(d) inset]. As detailed below, the charge transfer in graphene layer provides clear evidence of the CDW proximity effect.

To investigate the charge transfer between the two materials at the interface, we calculate the band structure of bare 1T-TaS_2 using the lattice-relaxed $\sqrt{13} \times \sqrt{13}$ CDW supercell as well as the G/TaS_2 heterostructure by placing 5x5 unit cells of graphene on top. The top and side views of the G/TaS_2 lattice model are depicted in Figs. 2(d) and (e), respectively. To take the strong correlation of Ta d-electrons into consideration, we perform generalized-gradient approximation plus on-site U (GGA+U) calculations with U=2.27eV for bare, monolayer 1T-TaS_2 in accordance with previous DFT calculations [25,26] as shown in Fig. 2(a). The CDW-induced isolated half-filled spin-degenerate flat band at E_F [see Fig. S4] splits into occupied spin up lower Hubbard band (LHB) and empty spin down upper Hubbard band (UHB) with a Mott gap of ~0.25eV in between. The on-site Hubbard U significantly enhances the Mott gap from ~0.12eV [see Fig. S5] to ~0.25eV [Fig. 2(a)] so that the UHB touches the lowest conduction bands, while experiments observe a localized Hubbard band more separated from the conduction band. This discrepancy implies the on-site Hubbard U of 2.27eV might be somewhat overestimated. Possible reasons are discussed below.

In the band structure of the G/TaS_2 heterostructure, both the 1T-TaS_2 Hubbard bands and the graphene Dirac cone are preserved [see Fig. 2(b)]. Compared to bare 1T-TaS_2, the Fermi level moves from the LHB up to the UHB due to the charge transfer from graphene to 1T-TaS_2. This is also accompanied with an energy shift of the graphene Dirac point from the Femi level E_F up to ~0.3eV above E_F at the K-point of the superstructure Brillouin zone [Fig. S3]. A careful comparison of the Dirac cone of G/TaS_2 with that of bare graphene leads us to conclude that the Fermi velocity is not changed by the proximity to 1T-TaS_2. The highly dispersive p_z-orbital derived Dirac cone intersects the CDW and Mott gaps and crosses both the dz^2-orbital derived narrow LHB and UHB. They indeed interact with each other, though in a gentle manner. Four small gaps of order 10meV emerge at the four crossing points as shown in the insets of Fig. 2(c). These small gaps which originate from the weak interlayer couplings

indicate finite hybridization between the Dirac and Hubbard states, giving rise to the proximity effect between graphene and 1T-TaS_2 as illustrated in Fig. 2(e).

Graphene is known to be a wide bandwidth semi-metal with high-mobility itinerant carriers. With graphene on top of 1T-TaS_2, there exists nontrivial charge transfer from graphene to 1T-TaS_2, as shown in the LDSA+U band structure in Fig. 2(b). These highly mobile electrons from graphene somewhat suppress the localized picture of the narrow Hubbard d-bands in 1T-TaS_2 and thus reduce the on-site U value of Ta. A comparison of the band structures for different U values with the STS results, suggests that the graphene layer screens the Coulomb interaction in 1T-TaS_2 and the Hubbard U of Ta is lowered by ~0.5eV due to the itinerant electrons in graphene. Therefore, we show in Fig. 2(c) the G/TaS_2 the band structure with a phenomenological value U=1.70eV, which reasonably reproduces the trend observed in the STS measurements (below).

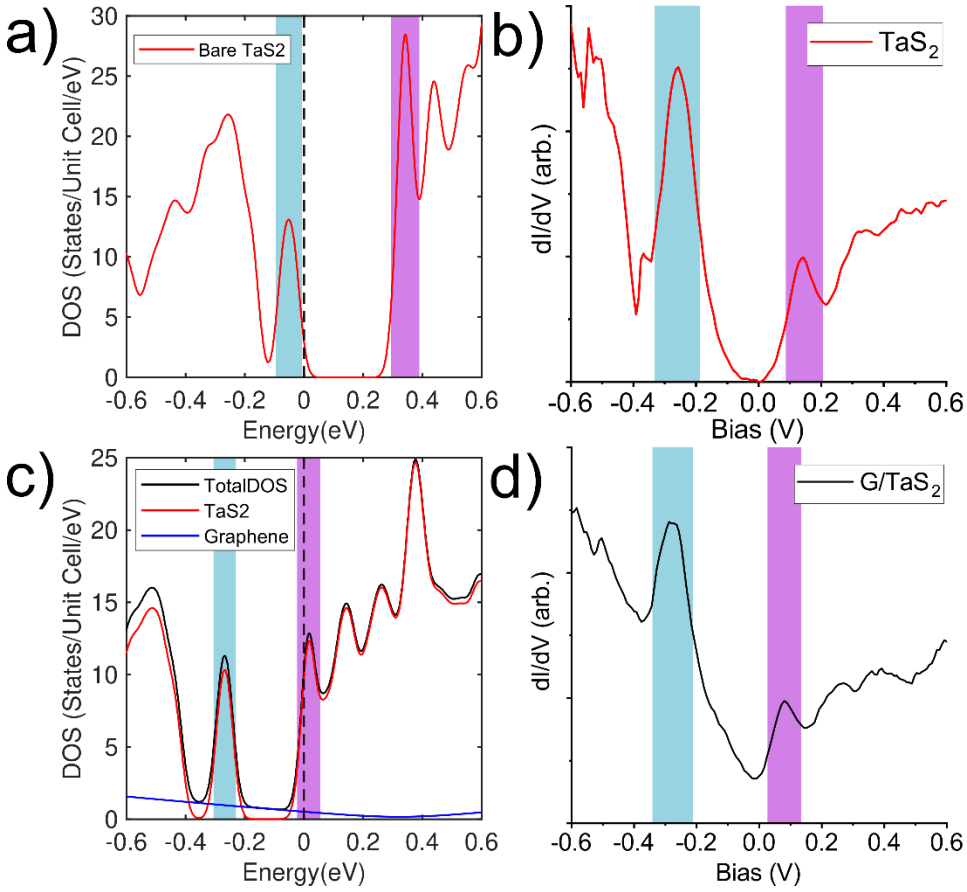

Figure 3: Density of States of Bare 1T-TaS_2 and G/1T-TaS_2 a) GGA+U calculated DOS of bare 1T-TaS_2 (U=2.27eV) b) Measured tunneling spectroscopy (STS) of the bare 1T-TaS_2 surface shows a gap at zero bias with peaks associated with upper and lower Hubbard bands (highlighted with violet and blue, respectively) in agreement with the calculated result (a). c) GGA+U calculated DOS of the G/TaS_2 heterostructure showing features resembling the Hubbard bands, conduction band, and valence band of 1T-TaS_2 with a reduced Mott-Hubbard interaction strength (U=1.70eV). The projected DOS (blue line) between the Hubbard-like bands originate from the Dirac cone states within the graphene layer d) Measured STS of G/1T-TaS_2 qualitatively agrees with the calculated result in (c), displaying Hubbard-like peaks, with a gap size that is reduced with respect to the Mott gap observed in bare 1T-TaS_2, and mid-

gap states which we associate with the graphene layer. Spectra in (b),(d) are taken at a set point of [V_b=1.2V, I_{SP}=80pA] with AC modulation $V_{AC} = 8mV$. Lower and upper Hubbard peaks are highlighted in blue and violet, respectively.

Next, we compare the calculated DOS with measured STS (proportional to the local DOS) on both the bare 1T-TaS_2 [Fig. 3(a),(b)] and graphene covered regions (Fig. 3c,d). GGA+U DOS of bare 1T-TaS_2 shown in Fig. 3(a) reflect the key features of the 1T-TaS_2 band structure in Fig. 2(a). The lower and upper Hubbard bands located respectively below E_F and ~0.35 eV above E_F with a ~0.35 eV Mott gap in between. The dips below LHB and above UHB indicate the scale of the CDW gap [Fig. S6]. These main features are consistent with those observed in our STS measurement [shown in Fig. 3(b)] which also show the expected Mott gap at the Fermi level flanked by lower and upper Hubbard peaks at -256mV and 144mV, respectively. Additionally, the two large dI/dV dips observed at -378mV and 218 mV are associated with the known CDW gap.

With graphene on top of 1T-TaS_2, the GGA+U DOS plotted in Fig. 3(c) also show UHB, LHB, Mott gap, and CDW gap similar to the DOS of bare 1T-TaS_2. The main differences from the bare 1T-TaS_2 case are i) the relative energies of the Fermi level, UHB, LHB, and Dirac point; ii) the linearly dispersing states within the Mott gap. Owing to the relatively stronger electron negativity of TaS_2, there exist notable charge transfer from graphene to 1T-TaS_2. Consequently, the Fermi level moves from the LHB top to the UHB bottom, meanwhile the graphene Dirac point shifts to a higher energy about 0.3eV above E_F. On the other hand, the mid-gap linear band comes from the Dirac cone states of the graphene cover layer. Because of the energy shift of the Dirac point to ~0.3eV above E_F, the V-shape DOS thus moves to ~0.3eV, leaving a linear-like band within the Mott gap below E_F.

The main features given from GGA+U are in good agreement with our STS results shown in Fig. 3(d). Two peaks near the Fermi level are labelled as lower and upper Hubbard bands (measured at -280mV and 88mV, respectively) with a V shaped DOS in between. Unlike the case of pristine, undoped graphene on an insulating substrate, here the DOS does not vanish at the Fermi level. The negative slope of the measured STS in between the Hubbard bands suggests the Dirac point in graphene has shifted to higher energies, indicative of the hole doping. We note that the GGA+U calculation of the DOS [Fig. 3(c)] is averaged over the entire heterostructure whereas the measured STS favors the region closest to the tip [Fig. 3(d)]. The preferential tunneling into the graphene top layer results in a larger mid-gap STS intensity (compared to Hubbard peak heights) than given by the calculation. Further modelling is needed to reproduce the relative spectral weights due to different orbitals within the vdW heterostructure as measured by an STM tip above the surface.

Comparing STS measurements of bare 1T-TaS_2 [Fig. 3(b)] and G/TaS_2 [Fig. 3(d)], we can see that the addition of the graphene layer induces both a shift of the Hubbard peaks as well as a reduction of the gap between them by approximately 7.5%. We interpret the reduction of the Mott gap size as being due to screening of the Coulomb interaction near the surface of 1T-TaS_2 by itinerant electrons in graphene, reducing U and the separation between Hubbard peaks. As mentioned above, we adopt a smaller on-site U=1.70eV in the calculation of the G/TaS_2 case to consider this screening effect observed in STS.

We note that taking a unit cell consisting of two layers of 1T-TaS_2 results in dimerization between layers, as suggested by recent theoretical and experimental works [27-30]. In this case, 1T-TaS_2 is no longer best described as a two-dimensional Mott insulator with magnetic ordering, but rather a band

insulator, as the formation of interlayer dimer singlets suppresses magnetism. We show in Supplemental Material [Fig. S7] that the main features of adding a graphene layer on top of one or two layers of 1T-TaS_2 are qualitatively similar to the single layer case, giving rise to a shift of E_F, reducing the gap size, and featuring charge transfer with the graphene layer. Our experimental technique is not sensitive to the spin-polarization; thus, we cannot identify the magnetic ground state of 1T-TaS_2 in this study. However, our calculations suggest that if a magnetic moment is present in 1T-TaS_2, the addition of the graphene layer will not suppress the moment at the surface. Therefore, measurements using graphene encapsulation and spin-polarized STM tips might be able to identify the magnetic properties of the 1T-TaS_2 surface in future measurements.

As mentioned above, the charge density map in Fig. 1(c) left panel shows the hole density in graphene induced by 1T-TaS_2, which corresponds to the local charge transfer from graphene to TaS_2. The missing electron density in graphene shows a clear correlation with the CDW pattern in 1T-TaS_2, indicating a proximity-induced CDW in graphene. Figure 2(e) demonstrates the real-space interlayer hybridization arising from the state around the Dirac-LHB crossing points in reciprocal space. The interlayer charge density overlap indicates that the graphene and 1T-TaS_2 layers are intimately connected by tunneling electrons, resulting in a novel proximity effect induced by charge transfer as discussed below.

The simplified Hamiltonian of the G/TaS_2 bilayer system is given by:

$$H = H_d + H_c + H_t,$$

$$H_d = \sum_{\langle i,j\rangle,\sigma} -t_{ij}^{d} d_{i,\sigma}^{\dagger} d_{j,\sigma} + h.c. - \sum_{\langle i',j'\rangle,\sigma} (\Delta_d^{CDW}(i',j'))^{*} d_{i',\sigma}^{\dagger} d_{j',\sigma} + h.c. + \sum_{\langle i',j'\rangle} \left|\Delta_d^{CDW}(i',j')\right|^2,$$

$$H_c = \sum_{\langle i,j\rangle,\sigma} -t_{ij}^{c} c_{i,\sigma}^{\dagger} c_{j,\sigma} + h.c. = \sum_{k,\sigma} (\epsilon_k - \mu) c_{k,\sigma}^{\dagger} c_{k,\sigma},$$

$$H_t = -t \sum_{i,\sigma} c_{i,\sigma}^{\dagger} d_{i,\sigma} + h.c.,$$

where H_d (H_c) stands for the simplified Hamiltonian of the 1T-TaS_2 (graphene) layer, respectively, and H_t describes a weak charge transfer (hopping) term between these two layers (we neglect a small mismatch in spatial locations between the nearest-neighbor sites of the corresponding layer). The insulating 1T-TaS_2 layer shows CDW order with the order parameter $\Delta_d^{CDW}(i',j') \equiv \sum_\sigma \langle d_{i',\sigma}^{\dagger} d_{j',\sigma} \rangle$ where i', j' are sites within the CDW unit cell. The graphene layer has the linear Dirac dispersion: $(\epsilon_k - \mu) \approx \hbar v_F |k - k_F|$. Here, i, j refer to the nearest-neighbor sites of the corresponding lattices, and $t_{ij}^{d(c)}$ refers to the nearest-neighbor tight-binding hoping terms on the 1T-TaS_2 (graphene) layer, respectively.

Via the second order perturbation in the H_t term of the CDW unit cell, the following exchange term $H_t^{(2)}$ is generated:

$$H_t^{(2)} = t^2 \sum_{\langle i',j'\rangle,\sigma,\sigma'} c_{i',\sigma}^\dagger d_{i',\sigma} d_{j',\sigma'}^\dagger c_{j',\sigma'} + h.c.$$

A simple mean-field decoupling of $H_t^{(2)}$ in terms of $\Delta_d^{CDW}(i',j')$ (considering only $\sigma = \sigma'$ and assuming spin-isotropic CDW order $\langle d_{j',\uparrow}^\dagger d_{j',\uparrow}\rangle = \langle d_{j',\downarrow}^\dagger d_{j',\downarrow}\rangle$) gives $H_t^{(2)} \to H_{t^2}^{MF}$ with:

$$H_{t^2}^{MF} \approx -t^2/2 \sum_{\langle i',j'\rangle,\sigma} (\Delta_d^{CDW}(i',j'))^* c_{i',\sigma}^\dagger c_{j',\sigma} - t^2/2 \sum_{\langle i',j'\rangle,\sigma} (\Delta_d^{CDW}(i',j'))^* \langle c_{i',\sigma}^\dagger c_{j',\sigma}\rangle + h.c.,$$

where the mean-field decoupling term ($\langle c_{i',\sigma}^\dagger c_{j',\sigma}\rangle\, d_{i',\sigma}^\dagger d_{j',\sigma}$) in $H_t^{(2)}$ is neglected since we expect $\left|\langle c_{i',\sigma}^\dagger c_{j',\sigma}\rangle\right| \ll \left|\langle d_{i',\sigma}^\dagger d_{j',\sigma}\rangle\right|$. The CDW proximity effect is manifested in $H_{t^2}^{MF}$ as a weak CDW order $\sum_\sigma \langle c_{i',\sigma}^\dagger c_{j',\sigma}\rangle$ is induced on the graphene layer by the second order charge transfer between the two layers with the following identification:

$$\Delta_c^{CDW}(i',j') \equiv -1/2 \sum\nolimits_\sigma \langle c_{i',\sigma}^\dagger c_{j',\sigma}\rangle^* = -t^2/2 \left(\Delta_d^{CDW}(i',j')\right)^*,$$

or equivalently, $\sum_\sigma \langle c_{i',\sigma}^\dagger c_{j',\sigma}\rangle = t^2 \Delta_d^{CDW}(i',j')$. Via the above identification, the Hamiltonian $H_{t^2}^{MF}$ can be expressed as:

$$H_{t^2}^{MF} = \sum_{\langle i',j'\rangle,\sigma} \Delta_c^{CDW}(i',j') c_{i',\sigma}^\dagger c_{j',\sigma} + h.c. + 2|\Delta_c^{CDW}(i',j')|^2,$$

which leads to $\Delta_c^{CDW}(i',j') = -1/2 \sum_\sigma \langle c_{i',\sigma}^\dagger c_{j',\sigma}\rangle^*$ identified above via minimizing the free energy associated with $H_{t^2}^{MF}$ with respect to $\Delta_c^{CDW}(i',j')$. Note that from above derivations, we indeed find that $\left|\langle c_{i',\sigma}^\dagger c_{j',\sigma}\rangle\right| \sim t^2 \left|\langle d_{i',\sigma}^\dagger d_{j',\sigma}\rangle\right| \ll \left|\langle d_{i',\sigma}^\dagger d_{j',\sigma}\rangle\right|$, as expected. Note also that the CDW order parameters induced on graphene layer shows the opposite sign with respect to that on 1T-TaS_2 layer, consistent with the hole-like (particle-like) CDW intensity on graphene (1T-TaS_2) layer obtained from DFT calculations, respectively. We emphasize here that the above mechanism based on charge transfer is distinct from all the previously realized proximity effects, including superconducting, magnetic and spin-orbit proximity effects.

In summary, we demonstrate, by STM/STS measurements and DFT calculations, the existence of a novel proximity-induced CDW in graphene resulting from the short-range exchange interaction with the CDW hosted by the 1T-TaS_2 crystal. Concomitant with the proximity induced CDW in graphene, which is out-of-phase with that in 1T-TaS_2, we observe a substantial reduction in the Mott gap of the 1T-TaS_2 crystal, indicating the presence of proximity-induced mid-gap carriers which screen the Mott-Hubbard interaction. These observations open intriguing possibilities for engineering correlations and manipulating charge carriers in heterostructures. They provide a new platform for non-linear electronic devices based on sliding, pinning, and phonon softening of the CDW induced within the graphene layer. Additional measurements including spin-resolved STM/STS, Raman spectroscopy, and electronic transport will further help elucidate the effects proposed in this work.

Methods: Samples were fabricated by mechanical exfoliation of graphene and separately TaS_2 flakes inside an argon-filled glovebox. The thin TaS_2 flake (2.4-24nm or 4-40 layers) was exfoliated from a bulk

1T-TaS_2 crystal, which was grown by iodine chemical vapor transport, and transferred onto a passivated SiO_2-capped degenerately doped Si wafer. The graphene and 1T-TaS_2 flakes were aligned vertically and brought into close contact with micromanipulators under an optical microscope and then heated to promote adhesion. Standard electron beam lithography and electrode deposition (4-5nm Ti/40-50nm Au) were used to make electrical contact to the sample [31]. After removing the PMMA mask the resulting heterostructure was annealed (180-220°C) in hydrogen/argon (10%/90%) to remove polymer residues [32]. STM and STS were performed using a homebuilt STM [33,34] at 78K in high-vacuum <10^{-5} Torr. At this temperature we partially remove the encapsulating graphene layer using the STM tip (mechanically cut Pt/Ir) resulting in a region that allows us to differentiate the properties of bare and graphene covered 1T-TaS_2 (see Supplementary Figure S1). We use an RHK R9 SPM controller for electronic control and data acquisition.

Acknowledgements

MAA was supported by the National Science Foundation grant EFRI 1433307; EYA and NT acknowledge support from the Department of Energy grant DOE-FG02-99ER45742 and the Gordon and Betty Moore Foundation EPiQS initiative grant GBMF9453; GL was supported by Rutgers University; CJW was supported by The National Research Foundation of Korea (NRF), grant No. 2016K1A4A4A01922028 and 2020M3H4A2084417; SWC was supported by the Betty Moore Foundation's EPiQS grant GBMF6402 and Rutgers University, C.-H. C. was supported by MOST (Grant NO.: 107-2112-M-009-010-MY3, 110-2112-M-A49-018-MY3) and the NCTS of Taiwan, R.O.C., J.H.T acknowledges support from the Ministry of Science and Technology, Taiwan under grant: MOST 109-2112-M-007 -034 -MY3, and from NCHC, CINC-NTU, AS-iMATE-109-13, and CQT-NTHU-MOE, Taiwan.

1 Geim, A. K. & Grigorieva, I. V. Van der Waals heterostructures. *Nature* **499**, 419-425, doi:10.1038/nature12385 (2013).

2 Levy, N. *et al.* Strain-Induced Pseudo-Magnetic Fields Greater Than 300 Tesla in Graphene Nanobubbles. *Science* **329**, 544-547 (2010).

3 Carrillo-Bastos, R. *et al.* Strained fold-assisted transport in graphene systems. *Physical Review B* **94**, 125422, doi:10.1103/PhysRevB.94.125422 (2016).

4 Jinhai Mao, S. P. M., Miša Anđelković, Xinyuan Lai, & Yang Cao, K. W., Takashi Taniguchi, Lucian Covaci, Francois M. Peeters, Andre K. Geim. Yuhang Jiang, Eva Y. Andrei. Evidence of Flat Bands and Correlated States in Buckled Graphene Superlattices. *Nature* **584** (2020).

5 Meissner, H. Superconductivity of Contacts with Interposed Barriers. *Physical Review* **117**, 672-680, doi:10.1103/PhysRev.117.672 (1960).

6 Hauser, J. J. Magnetic Proximity Effect. *Physical Review* **187**, 580-583, doi:10.1103/PhysRev.187.580 (1969).

7 Zhao, R. *et al.* Tuning Phase Transitions in 1T-TaS2 via the Substrate. *Nano Letters* **17**, 3471-3477, doi:10.1021/acs.nanolett.7b00418 (2017).

8 Frano, A. *et al.* Long-range charge-density-wave proximity effect at cuprate/manganate interfaces. *Nature Materials* **15**, 831-834, doi:10.1038/nmat4682 (2016).

9 Li, A. J., Zhu, X., Stewart, G. R. & Hebard, A. F. Bi-2212/1T-TaS2 Van der Waals junctions: Interplay of proximity induced high-Tcsuperconductivity and CDW order. *Scientific Reports* **7**, 4639, doi:10.1038/s41598-017-04645-1 (2017).
10 Dreher, P. *et al.* Proximity Effects on the Charge Density Wave Order and Superconductivity in Single-Layer NbSe2. *ACS Nano*, doi:10.1021/acsnano.1c06012 (2021).
11 Du, X., Skachko, I. & Andrei, E. Y. Josephson current and multiple Andreev reflections in graphene SNS junctions. *Phys. Rev B* **77** (2008).
12 Heersche, H. B., Jarillo-Herrero, P., Oostinga, J. B., Vandersypen, L. M. K. & Morpurgo, A. F. Bipolar supercurrent in graphene. *Nature* **446**, 56-59, doi:10.1038/nature05555 (2007).
13 Avsar, A. *et al.* Spin-orbit proximity effect in graphene. *Nat Commun* **5**, 4875, doi:10.1038/ncomms5875 (2014).
14 Liang, X. *et al.* The magnetic proximity effect and electrical field tunable valley degeneracy in MoS2/EuS van der Waals heterojunctions. *Nanoscale* **9**, 9502-9509, doi:10.1039/c7nr03317f (2017).
15 Heersche, H. B., Jarillo-Herrero, P., Oostinga, J. B., Vandersypen, L. M. & Morpurgo, A. F. Bipolar supercurrent in graphene. *Nature* **446**, 56-59, doi:10.1038/nature05555 (2007).
16 Keimer, B., Kivelson, S. A., Norman, M. R., Uchida, S. & Zaanen, J. From quantum matter to high-temperature superconductivity in copper oxides. *Nature* **518**, 179-186, doi:10.1038/nature14165 (2015).
17 Lin, D. *et al.* Patterns and driving forces of dimensionality-dependent charge density waves in 2H-type transition metal dichalcogenides. *Nat Commun* **11**, 2406, doi:10.1038/s41467-020-15715-w (2020).
18 Chen, C., Singh, B., Lin, H. & Pereira, V. M. Reproduction of the Charge Density Wave Phase Diagram in 1T-$TiSe_2$ Exposes its Excitonic Character. *Physical Review Letters* **121**, 226602, doi:10.1103/PhysRevLett.121.226602 (2018).
19 Zhang, K. *et al.* Evidence for a Quasi-One-Dimensional Charge Density Wave in CuTe by Angle-Resolved Photoemission Spectroscopy. *Physical Review Letters* **121**, 206402, doi:10.1103/PhysRevLett.121.206402 (2018).
20 Kresse, G. & Furthmüller, J. Efficiency of ab-initio total energy calculations for metals and semiconductors using a plane-wave basis set. *Computational Materials Science* **6**, 15-50, doi:https://doi.org/10.1016/0927-0256(96)00008-0 (1996).
21 Kresse, G. Ab initio molecular dynamics for liquid metals. *Journal of Non-Crystalline Solids* **192-193**, 222-229, doi:https://doi.org/10.1016/0022-3093(95)00355-X (1995).
22 Kresse, G. & Furthmüller, J. Efficient iterative schemes for ab initio total-energy calculations using a plane-wave basis set. *Physical Review B* **54**, 11169-11186, doi:10.1103/PhysRevB.54.11169 (1996).
23 Perdew, J. P. *et al.* Atoms, molecules, solids, and surfaces: Applications of the generalized gradient approximation for exchange and correlation. *Physical Review B* **46**, 6671-6687, doi:10.1103/PhysRevB.46.6671 (1992).
24 Perdew, J. P. & Wang, Y. Pair-distribution function and its coupling-constant average for the spin-polarized electron gas. *Physical Review B* **46**, 12947-12954, doi:10.1103/PhysRevB.46.12947 (1992).
25 Darancet, P., Millis, A. J. & Marianetti, C. A. Three-dimensional metallic and two-dimensional insulating behavior in octahedral tantalum dichalcogenides. *Physical Review B* **90**, 045134, doi:10.1103/PhysRevB.90.045134 (2014).
26 Qiao, S. *et al.* Mottness Collapse in 1T−TaS2−xSex Transition-Metal Dichalcogenide: An Interplay between Localized and Itinerant Orbitals. *Physical Review X* **7**, 041054, doi:10.1103/PhysRevX.7.041054 (2017).

27 Ngankeu, A. S. *et al.* Quasi-one-dimensional metallic band dispersion in the commensurate charge density wave of 1T-TaS_2. *Physical Review B* **96**, 195147, doi:10.1103/PhysRevB.96.195147 (2017).
28 Ritschel, T., Berger, H. & Geck, J. Stacking-driven gap formation in layered 1T-TaS2. *Physical Review B* **98**, 195134, doi:10.1103/PhysRevB.98.195134 (2018).
29 Lee, S. H., Goh, J. S. & Cho, D. Origin of the Insulating Phase and First-Order Metal-Insulator Transition in 1T-TaS_2. *Phys Rev Lett* **122**, 106404, doi:10.1103/PhysRevLett.122.106404 (2019).
30 Butler, C. J., Yoshida, M., Hanaguri, T. & Iwasa, Y. Mottness versus unit-cell doubling as the driver of the insulating state in 1T-TaS2. *Nat Commun* **11**, 2477, doi:10.1038/s41467-020-16132-9 (2020).
31 Luican-Mayer, A. *et al.* Negative differential resistance observed on the charge density wave of a transition metal dichalcogenide. *Nanoscale* **11**, 22351-22358, doi:10.1039/c9nr07857f (2019).
32 Wang, Z. *et al.* Surface-Limited Superconducting Phase Transition on 1 T-TaS2. *ACS Nano* **12**, 12619-12628, doi:10.1021/acsnano.8b07379 (2018).
33 Li, G., Luican, A. & Andrei, E. Y. Scanning Tunneling Spectroscopy of Graphene on Graphite. *Physical Review Letters* **102**, 176804, doi:10.1103/PhysRevLett.102.176804 (2009).
34 Li, G., Luican, A. & Andrei, E. Y. Self-navigation of a scanning tunneling microscope tip toward a micron-sized graphene sample. *Review of Scientific Instruments* **82**, 073701, doi:10.1063/1.3605664 (2011).

Supplementary Files

This is a list of supplementary files associated with this preprint. Click to download.

- SupportingInformation22212.pdf